# High-response formamidine bromide lead hybrid cadmium sulfide photodetector

Yao Liu (刘 耀)[1], Lei Liu (刘 磊)[1], Ruifeng Zhang (张锐峰)[1], Weiye Yang (杨伟业)[1], and Yingkai Liu (刘应开)[2,3,*]

[1] Institute of Physics and Electronic Information, Yunnan Normal University, Kunming 650500, China

[2] Yunnan Key Laboratory of Optoelectronic Information Technology, Kunming 650500, China

[3] Key Laboratory of Advanced Technique & Preparation for Renewable Energy Materials, Ministry of Education, Yunnan Normal University, Kunming 650500, China

Organic–inorganic hybrid perovskite formamidinium lead bromide nanosheet (FAPbBr$_3$ NS) is regarded as a superior substance used to construct optoelectronic devices. However, its uncontrollable stability seriously affects its application in the field of photodetectors. In this paper, FAPbBr$_3$ is combined with cadmium sulfide nanobelt (CdS NB) to construct a hybrid device that greatly improves the stability and performance of the photodetector. The response of the FAPbBr$_3$ NS/CdS NB detector under 490 nm light illumination reaches 5712 A/W, while the response of the FAPbBr$_3$ photodetector under equivalent conditions is only 25.45 A/W. The photocurrent of the FAPbBr$_3$ NS/CdS NB photodetector is nearly 80.25% of the initial device after exposure to air for 60 days. The difference in electric field distribution between the single material device and the composite device is simulated by the finite-difference time-domain method. It shows the advantages of composite devices in photoconductive gain and directly promotes the hybrid device performance. This paper presents a new possibility for high stability, fast response photodetectors.

**Keywords:** organic–inorganic hybrid perovskite; stability; finite-difference time-domain; photodetector.

**DOI:** 10.3788/COL202422.022502

## 1. Introduction

During the last decade, organic–inorganic hybrid chalcogenides have attracted intense attention as a consequence of their excellent optical properties, such as high optical absorption coefficients[1–3], carrier mobility, and long carrier diffusion[4,5]. These intrinsic features make them attractive for various applications, including photodetectors[6–8], solar cells[9], LEDs[10–12], and laser devices[12]. Compared with CsPbBr$_3$ and MAPbBr$_3$, FAPbBr$_3$ has pure green light emission and better chemical stability[2]. Recently, Li *et al.* used FAPbBr$_3$ as high-performance photodetector[13]. The Zeng group has fabricated FAPbBr$_3$ perovskite nanoparticles by an ion exchange mediated self-assembly method[14]. Research revealed that FAPbBr$_3$ is a potential candidate for optoelectronic devices due to its longer carrier lifetime and diffusion lengths[15].

Cadmium sulfide (CdS) is one of the most excellent II–VI semiconductors with a direct bandgap (~2.42 eV), thermal and chemical stability, a high refractive index, and a relatively low work function. The design and manufacture of CdS photodetectors based on nanowires[16], nanoribbons[17], and

nanorods[18] have been investigated. In past years, researchers employed inorganic CdS, CdSe as well as SnO$_2$ to mediate optoelectronic performance of organic perovskites[19,20]. Compared with other inorganic materials, CdS has higher responsivity and a larger on/off ratio, and the photoelectric performance of CdS hybrid devices is better than that of CdSe and other materials[21–23]. Moreover, there are few reports on hybrid devices with formamidinium lead bromide nanosheet (FAPbBr$_3$ NS). Therefore, we choose CdS to mediate organic–inorganic hybrid perovskites.

In this work, we prepared FAPbBr$_3$ NS by the solution method and CdS nanobelt (NB) by PVD. FAPbBr$_3$ NS/CdS NB detector was successfully constructed, and its optoelectronic property was measured. It was found that it exhibits an outstanding responsivity of 5712 A/W and on/off ratio of $5.92 \times 10^4$, originating from the high photoelectric conversion efficiency of FAPbBr$_3$ NS. Exposure to the atmosphere with 50% humidity and 25°C, it was found that the undergone optimization perovskite device demonstrated a sustained performance retention of 80.25% over a period of 60 days.

## 2. Experimental Section

### 2.1. Preparation of FAPbBr$_3$ NS and CdS NB

0.5 mmol (62.5 mg) FABr and 0.5 mmol (183.4 mg) PbBr$_2$ was added to 1 mL mixed solution of dimethyl sulfoxide (DMSO) and N,N-dimethylformamide (DMF) with the ratio of 7:3 (DMSO to DMF) and stirred for 6 h at 60°C. After that, the precursor solution was filtered by a 0.24 µm polytetrafluoroethylene needle filter and 2.5 µL of FAPbBr$_3$ solution was extracted, added dropwise to 10 mm × 10 mm Si/SiO$_2$ substrate and then dried on a heating table at 40°C for 24 h. FABr and PbBr$_2$ were purchased from Polymer Light Technology Corp., Xi'an.

The synthesis of CdS NBs was conducted using a tube furnace containing a quartz tube with a diameter of 25 mm. Initially, a ceramic container with an adequate quantity of CdS powder was positioned at the center of the quartz tube. Subsequently, silicon (Si) wafers that had been subjected to a cleaning process were coated with gold particles by a sputtering technique for a duration of 100 s. These coated wafers were then positioned at both the upstream and downstream ends of the quartz tube. Subsequently, the adequately filled quartz tubes were moved to a tube furnace, wherein the temperature was initially elevated to 300°C for a duration of 30 min. Following this, the quartz tubes were kept at this temperature for 10 min and then the temperature was gradually increased to 835°C at a rate of 8°C/min and sustained at this level for 60 min. In the entire operation, the quartz tube was filled with argon gas, which contained 5% (volume fraction) hydrogen (H$_2$) at a flow rate of 15 standard cubic centimeters per minute (sccm).

### 2.2. Fabrication of FAPbBr$_3$ NS/CdS NB photodetector

First, Ti/Au electrodes (5/45 nm) were fabricated on SiO$_2$/Si substrates by electron beam evaporation, and then the grown FAPbBr$_3$ nanosheets were transferred to the electrodes by the PDMS-assisted dry method. Therewith, CdS NB was dispersed onto a clean substrate, adhesive CdS NB with PDMS film, and transferred to FAPbBr$_3$ NS to complete the device preparation; finally, the device underwent annealing at a temperature of 100°C for a duration of 10 min.

## 3. Results and Discussion

A scanning electron microscope (SEM) image of a single FAPbBr$_3$ NS is shown in Fig. 1(a). The NSs form an asymmetric polygon. Figure 1(b) shows an AFM image of FAPbBr$_3$ with a thickness of 150 nm. Figures 1(c) and 1(d) display SEM images of CdS NBs. It can be seen that the width of CdS NBs is about 10 µm and the thickness is about 70 nm. X-ray diffraction (XRD) was employed to reveal the crystal structures of FAPbBr$_3$ NS and CdS NBs, as depicted in Fig. 2. The diffraction peaks of CdS NBs are presented in Fig. 2(a). The $2\theta$ peaks are situated at 24.83°, 26.53°, 28.21°, 36.66°, 43.73°, 47.89°, 50.94°, 51.88°, 52.86°, and 58.35° corresponding to (100), (002), (101), (102), (110) (103), (200), (112), (201), (004), and (104) crystal planes, respectively, in good agreement with the standard card (standard card JCPDS No. 77-2306). This suggests that the prepared CdS NBs in this study exhibit a high degree of crystallinity and possess a pure crystalline phase. The XRD pattern of FAPbBr$_3$ NS is
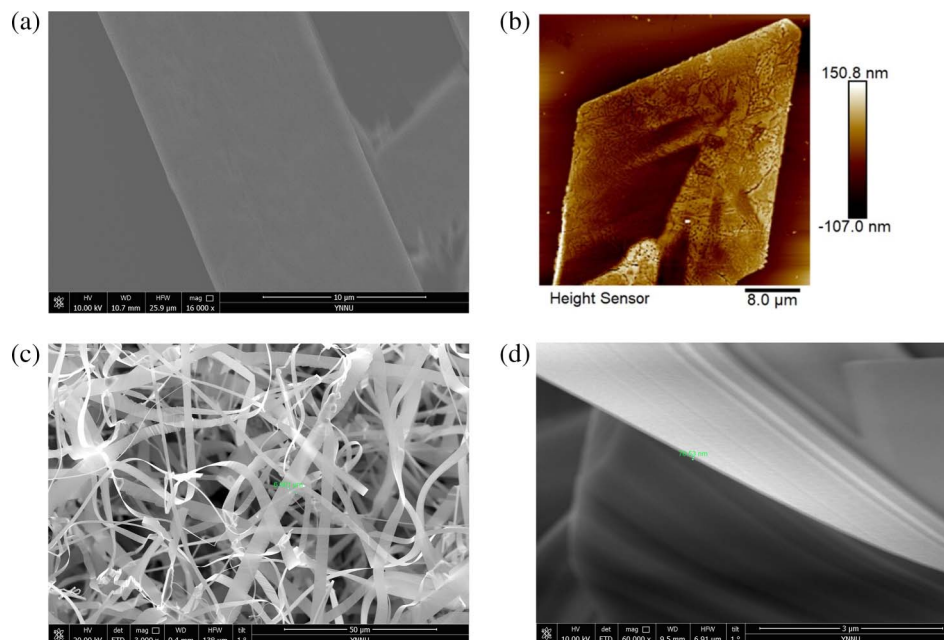


**Fig. 1.** SEM and AFM images of FAPbBr$_3$ NS and CdS NBs. (a) SEM image of FAPbBr$_3$ nanosheet; (b) AFM image of a single FAPbBr$_3$ nanosheet; (c) SEM image of CdS NBs; (d) cross section of CdS NBs.
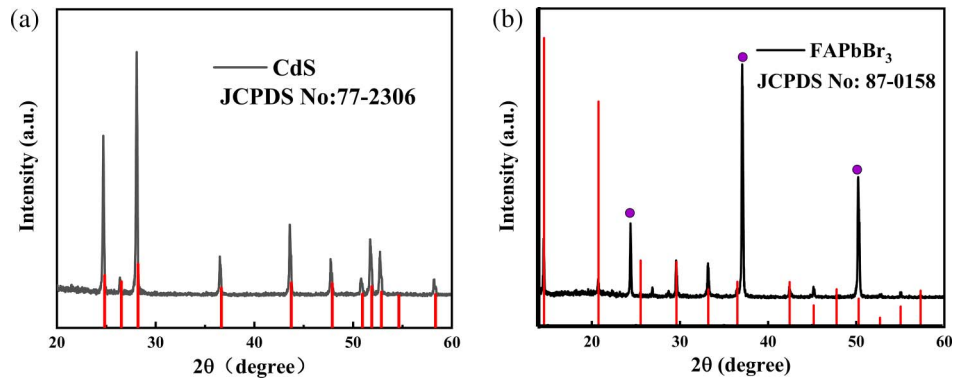
**Fig. 2.** XRD patterns of the samples: (a) CdS NBs; (b) FAPbBr$_3$ NSs.

illustrated in Fig. 2(b). The $2\theta$ peaks at 14.52°, 20.72°, 29.58°, 33.18°, 42.45°, and 45.26 ° match with (100), (110), (200), (211), (220), and (300) crystal planes (standard card JCPDS No. 87-0158). These results are also in agreement with those reported elsewhere[24,25]. The $2\theta$ peaks at 24.39°, 39.06°, and 50.21° marked by purple dots correspond to the (011), (212), and (211) crystal planes of SiO$_2$ (standard card JCPDS No. 82-1566), as shown in Fig. 2(b); the preparation of FAPbBr$_3$ NSs is on the Si substrate with 500 nm-thick SiO$_2$ layer.

The spectral response of the CdS NB/FAPbBr$_3$ heterostructure was investigated. Figure 3(a) shows UV-Vis absorption spectra of FAPbBr$_3$ and CdS NB/FAPbBr$_3$ hybrid structures

in the range of 300–800 nm. According to Tauc's[26] diagram, it is represented by the following equation:

$$(ah\nu)^{1/n} = A(h\nu - E_g),$$

where $\alpha$ is the absorption coefficient, $h$ is Planck's constant, $\nu$ is the frequency of light, $A$ is the proportionality constant, and $E_g$ is the bandgap. $n$ is one-half for the direct bandgap. The calculated bandgap of FAPbBr$_3$ is 2.24 eV in Fig. 3(b). The highest absorption of the hybrid FAPbBr$_3$ NS/CdS NB structure is located at 490 nm, whereas the hybrid structure exhibits a much improved
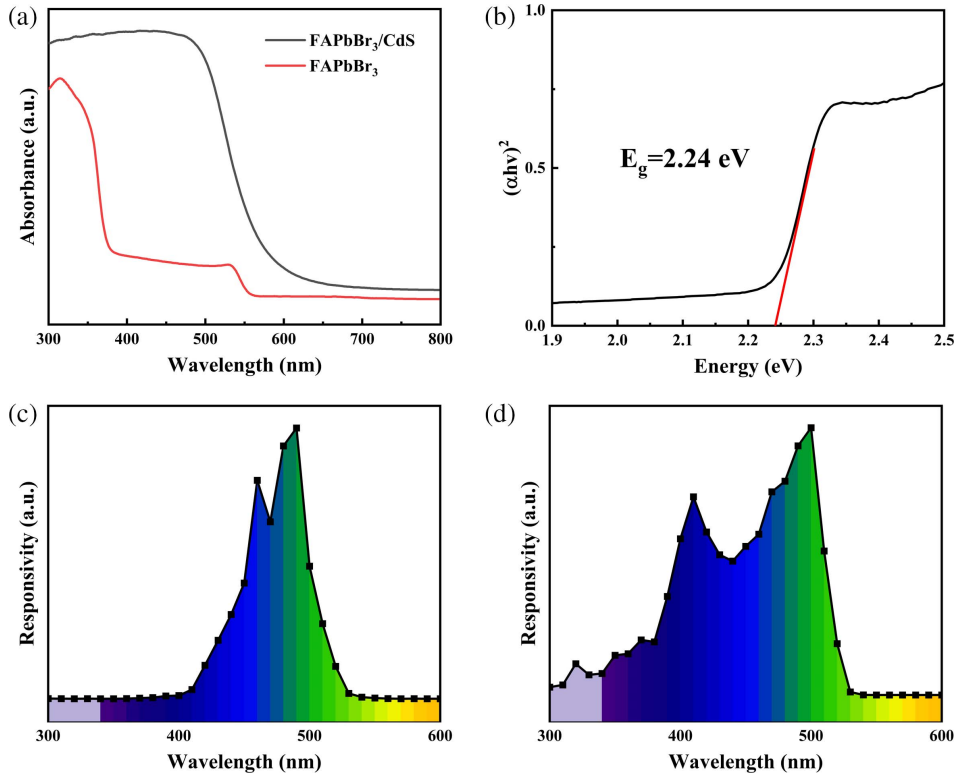


**Fig. 3.** Spectral response of FAPbBr$_3$ NS/CdS NB hybrid structure. (a) UV-Vis absorption spectra; (b) $(\alpha h\nu)^2$ versus photon energy curve of FAPbBr$_3$ NS; (c) and (d) spectral response of FAPbBr$_3$ NS device and FAPbBr$_3$ NS/CdS NB hybrid structures at a bias voltage of 5 V.

absorption rate in the range of 300 to 530 nm in Fig. 3(a). It was found that there are two descending platforms in the absorption spectrum of FAPbBr$_3$. The first peak at 350 nm corresponds to the absorption of PbBr$_2$ due to the extra PbBr$_2$ in the preparation of FAPbBr$_3$ for UV-Vis absorption measurement. The second peak at 530 nm originated from FAPbBr$_3$. Therefore, two descending platforms are formed in the absorption spectrum of FAPbBr$_3$. This phenomenon may be attributed to the coupled light absorption of CdS NBs and FAPbBr$_3$ NS. The enhanced absorption is advantageous for the performance of FAPbBr$_3$ NSs/CdS NBs hybrid devices. To better understand the response of FAPbBr$_3$ and FAPbBr$_3$ NS/CdS NB hybrid structures, the responsive curves of the two structures were measured in the range of 300–600 nm, respectively, as displayed in Figs. 3(c) and 3(d). It can be seen that the FAPbBr$_3$ NS/CdS NB hybrid structure has a broad responsive band at the wavelength of 400–500 nm, with two peaks located at 400 and 490 nm.

Figures 4(a) and 4(b) show the device schematic diagram of the FAPbBr$_3$ NS and FAPbBr$_3$ NS/CdS NB device. Figures 4(c) and 4(d) are their corresponding SEM images. Figure 4(c) shows the effective area of devices is 191.34 µm$^2$. It is clearly seen that CdS is covered on FAPbBr$_3$, and the effective area of the device is 293 µm$^2$ in Fig. 4(d). Their photoelectric properties will be systematically investigated at 490 nm and a power density of 138 µW/cm$^2$, as described in Figs. 4(e) and 4(f). The photocurrent and dark current of the hybrid FAPbBr$_3$ NS/CdS NB device (FAPbBr$_3$ NS one) at a bias voltage of 5 V are 1.19 µA (2.01 nA) and 20.1 pA (22.64 pA) with an on/off ratio of

$5.92 \times 10^4$ ($2.107 \times 10^2$). The on/off ratio of the front is $2.81 \times 10^2$ times as large as that of the latter. Figures 5(a) and 5(b) show $I$-$V$ curves of the FAPbBr$_3$ and FAPbBr$_3$ NS/CdS NB devices at 490 nm under light irradiation with different power densities. The observed trend indicates that there is a positive correlation between the power density and photocurrent, indicating that the effectiveness of the photocarriers is directly proportional to the quantity of photons absorbed. The photocurrent versus optical power density curve is plotted and fitted as $I = AP^\theta$, where $I$, $A$, and $P$ are the photocurrent, proportionality constant, and incident light intensity, respectively. The exponent $\theta$ determines the photocurrent response of the device toward light intensity. The fitted values of $\theta$ are 0.889 and 0.959 for FAPbBr$_3$ and FAPbBr$_3$ NS/CdS NB devices, respectively, as illustrated in Figs. 5(c) and 5(d). They are slightly less than the ideal value of 1, revealing that FAPbBr$_3$ NS and FAPbBr$_3$ NS/CdS NB devices have excellent optical exchange capability and have fewer defects. To further compare the performance of FAPbBr$_3$ NS and FAPbBr$_3$ NS/CdS NB detectors, the responsivity ($R$), external quantum efficiency (EQE), and specific detectivity ($D^*$) are evaluated by the following formula[7,8,27–29]:

$$R = \frac{I_{\text{light}} - I_{\text{dark}}}{P_0 \times A}, \quad D^* = \frac{R\sqrt{A}}{\sqrt{2eI_{\text{dark}}}}, \quad \text{EQE} = R\frac{\hbar c}{e\lambda},$$

where $I_{\text{light}}$ is the photocurrent, $I_{\text{dark}}$ is the dark current, $P_0$ is the incident light intensity, $A$ is the effective illuminance area, $e$ is
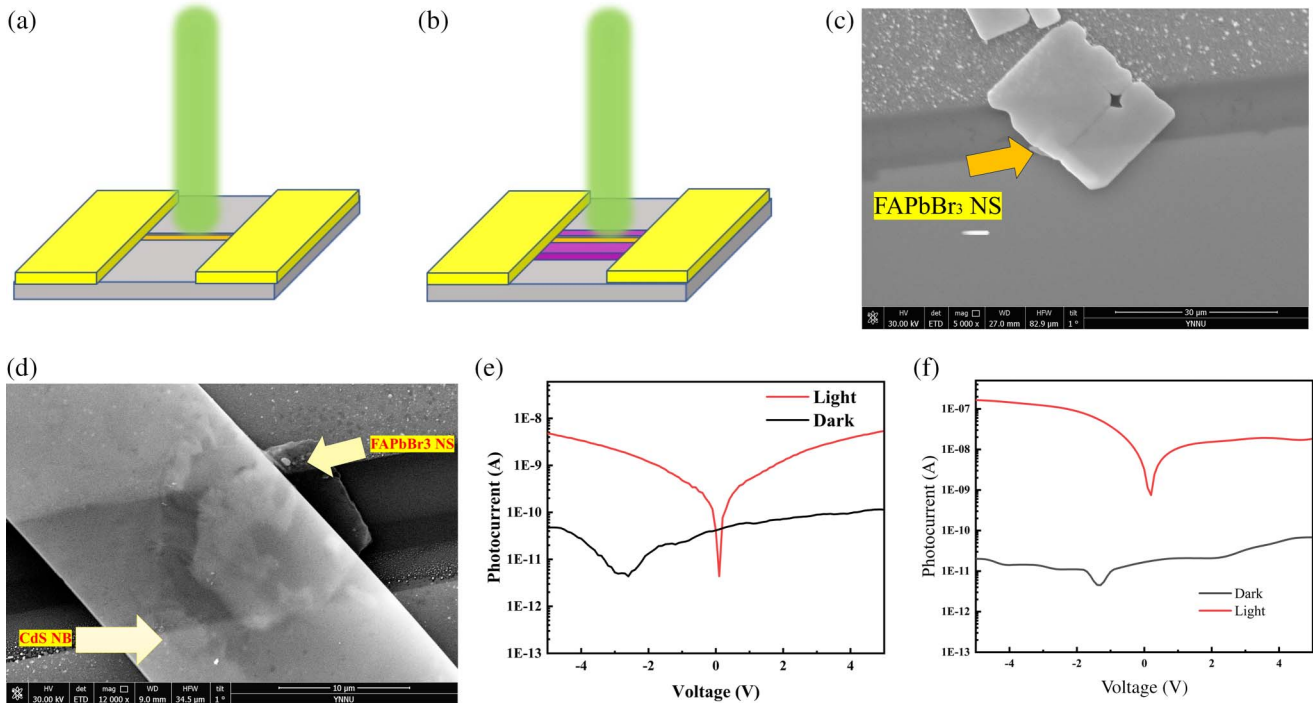


**Fig. 4.** (a) Schematic diagram of single FAPbBr$_3$ NS and (b) FAPbBr$_3$ NS/CdS NB hybrid structure device; (c), (d) SEM images of single FAPbBr$_3$ NS and FAPbBr$_3$ NS/CdS NB hybrid structure device, respectively; (e), (f) $I$-$V$ curves of a single FAPbBr$_3$ NS device and FAPbBr$_3$ NS/CdS NB device under 490 nm light irradiation, respectively.
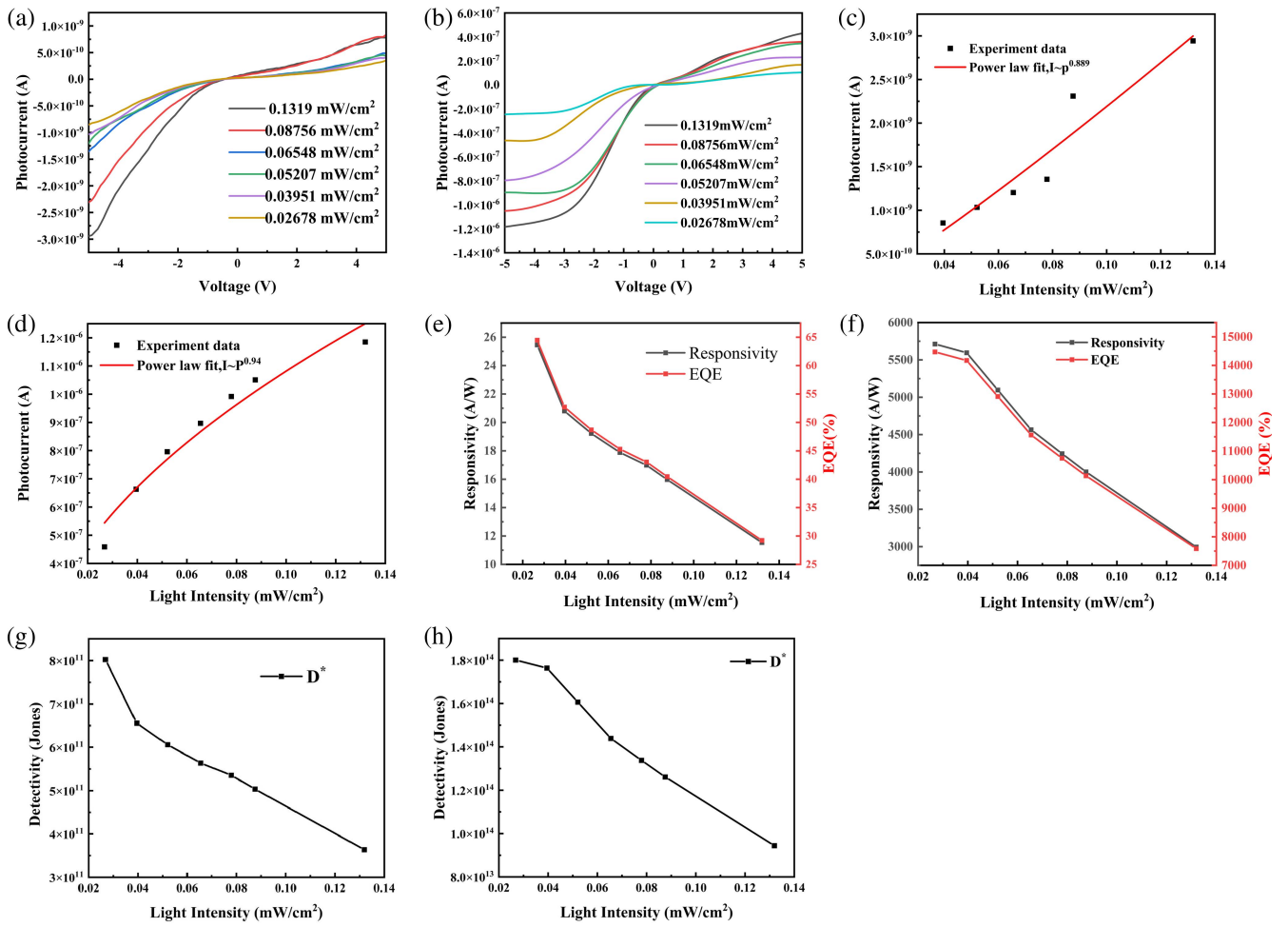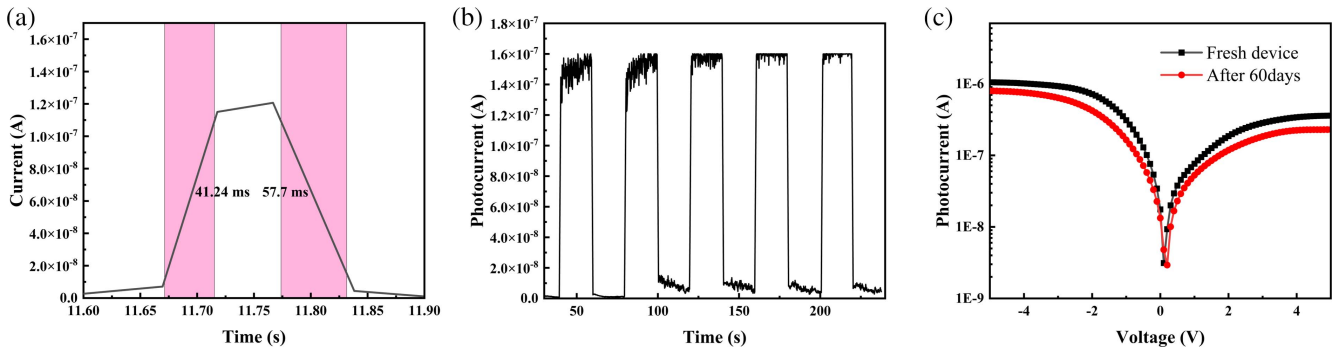
**Fig. 5.** Performance of FAPbBr$_3$ NS/CdS NB photodetector. (a) and (b) *I–V* curves; (c) and (d) photocurrent versus optical power density; (e), (f) EQE and (g), (h) *D** of single FAPbBr$_3$ NS device and CdS NB/FAPbBr$_3$ NS hybrid devices with increased light intensity under 490 nm laser at a bias voltage of 5 V.

the electron charge, $\hbar$ is Planck's constant, and $c$ and $\lambda$ are the velocity and wavelength of the incident light, respectively.

Based on the above equations, we obtained $R$, EQE, and $D^*$ of FAPbBr$_3$ and FAPbBr$_3$ NS/CdS NB detectors. The relationships of $R$, EQE, and $D^*$ versus power density are depicted in Figs. 5(e), 5(f), 5(g), and 5(h). It is exhibited that the maximum $R$, EQE,

and $D^*$ for the single FAPbBr$_3$ photodetector are 25.45 A/W, 64.5%, and $8.024 \times 10^{11}$ Jones. The maximum $R$, EQE, and $D^*$ of the FAPbBr$_3$ NS/CdS NB hybrid detector are $5.712 \times 10^3$ A/W, $1.45 \times 10^4$%, and $1.8 \times 10^{14}$ Jones, at least being 2 orders of magnitude higher than that of the single FAPbBr$_3$ NS one.



**Fig. 6.** *I–t* characteristic curve of FAPbBr$_3$ NS/CdS NB photodetector. (a) Rising and falling edges of a single cycle with 5 V voltage offset; (b) photocurrent variation with time of CdS NB/FAPbBr$_3$ NS hybrid device; (c) photocurrent of the device.

**Table 1.** Comparison of the Proposed Photodetector with Other Reported Devices in Terms of Photoresponse Parameters.

| Device Structure | On/Off Ratio | Responsivity (A/W) | EQE (%) | $D^*$ (Jones) | Rise/Decay Time | Ref. |
|---|---|---|---|---|---|---|
| 2D (OA) $2FA_{n-1}Pb_nBr_{3n+1}$ | – | 32 | – | – | 0.25/1.45 ms | [30] |
| FAPbBr$_3$ microcrystal | – | $4 \times 10^4$ | – | $3.87 \times 10^{14}$ | 0.67/0.75 ms | [31] |
| FAPbBr$_3$ QDs/graphene | – | $1.15 \times 10^5$ | $3.42 \times 10^7$ | – | 58/60 ms | [32] |
| MA$_{0.7}$FA$_{0.3}$PbBr$_3$ | $10^5$ | 0.51 | | $4.0 \times 10^{12}$ | 6.7/2.5 ms | [33] |
| FAPbI$_3$ | $1.4 \times 10^3$ | 3.27 | 630 | $1.35 \times 10^{12}$ | 0.35/0.54 ms | [34] |
| a-FAPbI$_3$ | $10^5$ | 11.46 | – | – | 5.4/10.9 ms | [13] |
| FAPbBr$_3$ NS/CdS NB | $5.92 \times 10^4$ | 5712 | $1.452 \times 10^4$ | $1.8 \times 10^{14}$ | 41.4/57.7 ms | This work |

One of the most important metrics for describing the photodetector is the response time. The rising and falling edges of the device are depicted in Fig. 6(a), in which the rise time (10% to 90% of the maximum current) and the decay time (90% to 10% of the maximum current) are calculated to be 41.42 and 57.7 ms,

respectively. Figure 6(b) shows *I-t* curves under an illumination of 490 nm with continuous on and off at bias voltages of 5 V. This told us about the reproducible and reversible photodetective behavior of the FAPbBr$_3$ NS/CdS NB device. The photocurrent of the device was 80.25% of that of the initial period in
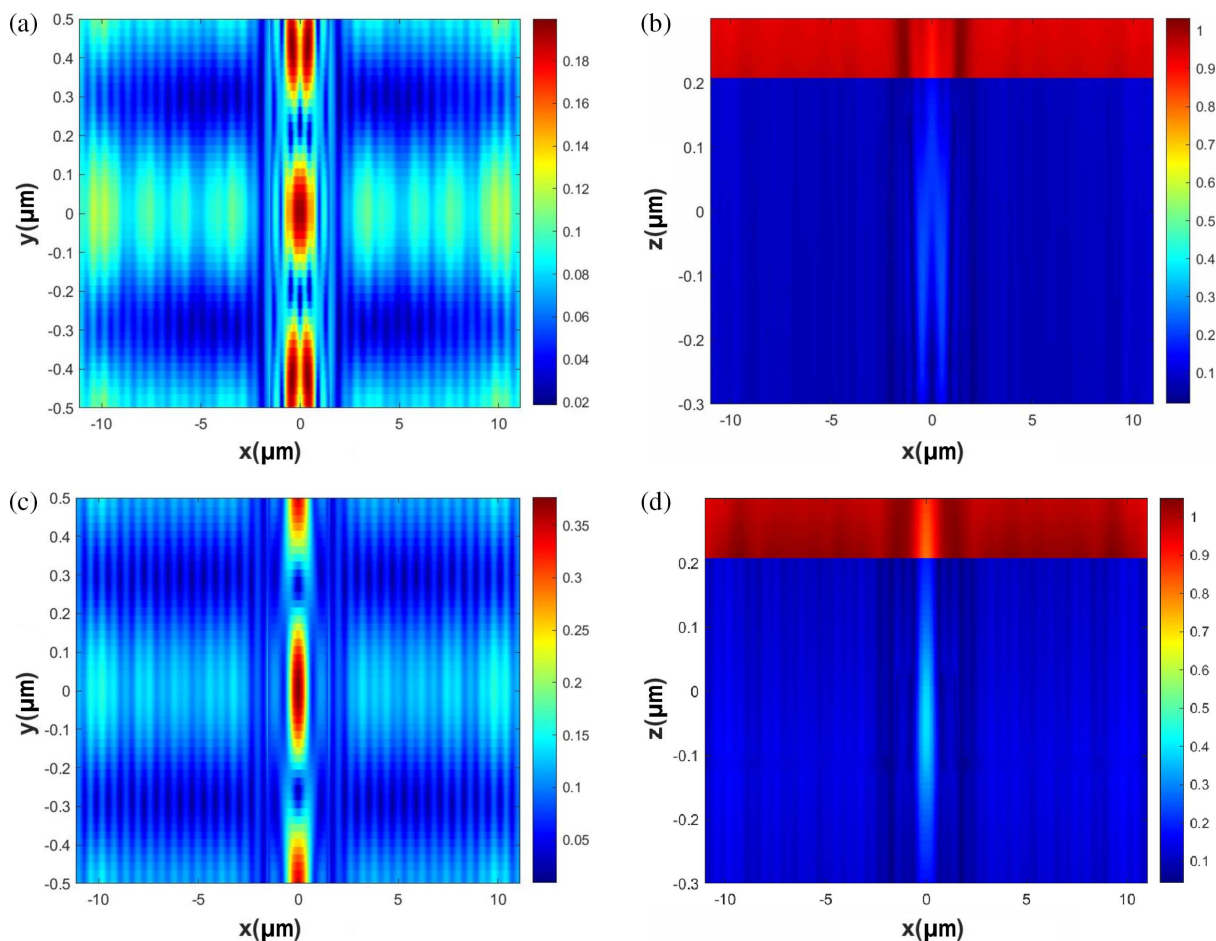


**Fig. 7.** (a) Simulated electric field density distribution of different structures under light irradiation at 490 nm and (b) electric field distribution of a single FAPbBr$_3$; (c) and (d) electric field distributions of the FAPbBr$_3$/CdS hybrid device.

Fig. 6(c), whereas the rise time/decay time is 42.18/58.04 ms after being stored in air for 60 days. The sensitivity of the device to light shows a weak attenuation.

To provide a better comparison, we summarize the photoelectric metrics of FA-based photodetector devices, as listed in Table 1. The device exhibited a notable enhancement in its photovoltaic performance, with some critical metrics experiencing an increase of at least 1 order of magnitude. Meanwhile, the FAPbBr$_3$ NS/CdS NB hybrid device is competitive with most FA-based photodetector devices, due to their better optoelectronic performance.

As the incident wavelength is larger than 530 nm, the responsivity of the device rapidly decreases, which is closely associated with the energy of the photon radiated. For the experiment, there will be a transition from impurities to the band. The energy of the photons absorbed by the electrons in the valence band of the FAPbBr$_3$ jumped to the conduction band, as the wavelength of the incident light is less than 530 nm. Under the effect of the internal electric field, the electrons and holes have different quasi-Fermi energy levels due to the generated electron–hole pairs by light. The hole concentration does not change, so the net free electron concentration increases[35]. To measure the photoelectric characteristic curve, the curve moves to the left. In order to elucidate the effect of geometry on optical properties and the optical response of the heterojunction devices, the distributions of electric field density in perovskite materials (150 nm in thickness)/CdS nanobelt (70 nm in thickness) heterostructures were estimated by numerical calculations using the FDTD method. In order to streamline the model, the dimensions of the perovskite were established as 5000 nm in length and 500 nm in breadth. In the data depicted in Fig. 7(a), the perovskite material exhibits localized regions of intense electric fields (commonly referred to as hot spots) inside its surface region upon exposure to 490 nm light. This observation implies that the perovskite has the capability to effectively restrict incident visible light. Importantly, this photo-limiting effect can be further enhanced by transferring[36] from the CdS belt to the surface of the perovskite. The augmentation in electric field intensity in the surface region of the nanostructure is readily apparent, leading to an increased efficacy in optical coupling and capture. The observed behavior may be comprehended due to the light-trapping effect often arising from the reflections occurring at the perimeters of the perovskite material. It is noteworthy that the optical characteristics of the aforementioned structures exhibit a high degree of consistency. In contrast to the single perovskite structure, it exhibits a shallow field penetration depth, resulting in a significantly restricted optical coupling capacity [Fig. 7(c)]. The theoretical simulation results are in good agreement with the optical response performance of the device. Figure 5(b) shows I-V curves of the perovskite/CdS NB heterostructure and the current-voltage curves of a single perovskite/CdS heterojunction under the same lighting irradiation. It is noted that the increase in photocurrent and stronger photovoltaic behavior may be due to the improved absorption of light by heterojunction with a larger area. Furthermore, the individual perovskite has inferior photoelectric characteristics to its limited

light absorption capability. Based on the aforementioned study, it can be concluded that the perovskite/CdS heterojunction possesses a superior option for attaining photodetectors with high-performance capabilities.

## 4. Conclusion

We have achieved the preparation of optoelectronic devices by transfer. The FAPbBr$_3$ NS/CdS NB heterojunction photodetector exhibits high response in the range of 400–530 nm. It was stored in air for 60 days and still had 80.25% of its original achievement. The optical responsivity, external quantum efficiency, and detection rate were $5.712 \times 10^3$ A/W, $1.45 \times 10^4$%, and $1.8 \times 10^{14}$ Jones, respectively, when the optical power was $26.78 \, \mu W/cm^2$ (at 490 nm). The response time of the photodetector in the 490 nm spectral range is short ($\sim$45 ms). Based on the photoelectric response mechanism, the photoelectric performance of the device is related to the efficiency of light capture and coupling, and the performance of the detector can be further improved by optimizing this method. The transfer of FAPbBr$_3$ to different substrates makes it an excellent candidate for different optoelectronic devices.

## References

1. F. Hao, C. C. Stoumpos, D. H. Cao, *et al.*, "Lead-free solid-state organic-inorganic halide perovskite solar cells," Nat. Photonics **8**, 489 (2014).
2. K. M. Boopathi, R. Mohan, T.-Y. Huang, *et al.*, "Synergistic improvements in stability and performance of lead iodide perovskite solar cells incorporating salt additives," J. Mater. Chem C **4**, 1591 (2016).
3. W. Shangguan, C. X. Yan, and J. M. Cai, "Quasi-planar tetracoordinate carbon networks with tunable electronic properties combined with ultra-high carrier mobility and optical absorption coefficient: two-dimensional Be$_2$C," Appl. Surf. Sci. **604**, 154644 (2022).
4. H. S. Kim, C. R. Lee, J. H. Im, *et al.*, "Lead iodide perovskite sensitized all-solid-state submicron thin film mesoscopic solar cell with efficiency exceeding 9%," Sci. Rep. **2**, 591 (2012).
5. Q. F. Dong, Y. J. Fang, Y. C. Shao, *et al.*, "Electron-hole diffusion lengths < 175 µm in solution-grown CH$_3$NH$_3$PbI$_3$ single crystals," Science **347**, 967 (2015).
6. S. A. Veldhuis, P. P. Boix, N. Yantara, *et al.*, "Perovskite materials for light-emitting diodes and lasers," Adv. Mater. **28**, 6804 (2016).
7. X. Liu, L. L. Gu, Q. P. Zhang, *et al.*, "All-printable band-edge modulated ZnO nanowire photodetectors with ultra-high detectivity," Nat. Commun. **5**, 4007 (2014).
8. S. X. Li, H. Xia, X. C. Sun, *et al.*, "Curved photodetectors based on perovskite microwire arrays via in situ conformal nanoimprinting," Adv. Funct. Mater. **32**, 2202277 (2022).
9. D. P. Mcmeekin, G. Sadoughi, W. Rehman, *et al.*, "A mixed-cation lead mixed-halide perovskite absorber for tandem solar cells," Science **351**, 151 (2016).

10. Z. G. Xiao, R. A. Kerner, L. F. Zhao, *et al.*, "Efficient perovskite light-emitting diodes featuring nanometre-sized crystallites," Nat. Photonics **11**, 108 (2017).

11. Q. Shan, J. Li, J. Song, *et al.*, "All-inorganic quantum-dot light-emitting diodes based on perovskite emitters with low turn-on voltage and high humidity stability," J. Mater. Chem. C **5**, 4565 (2017).

12. L. Meng, E. P. Yao, Z. R. Hong, *et al.*, "Pure formamidinium-based perovskite light-emitting diodes with high efficiency and low driving voltage," Adv. Mater. **29**, 1603826 (2017).

13. S. G. Li, S. C. Tong, J. L. Yang, *et al.*, "High-performance formamidinium-based perovskite photodetectors fabricated via doctor-blading deposition in ambient condition," Org. Electron. **47**, 102 (2017).

14. D. J. Yu, F. Cao, Y. J. Gao, *et al.*, "Room-temperature ion-exchange-mediated self-assembly toward formamidinium perovskite nanoplates with finely tunable, ultrapure green emissions for achieving Rec. 2020 displays," Adv. Funct. Mater. **28**, 1800248 (2018).

15. A. A. Zhumekenov, M. I. Saidaminov, M. A. Haque, *et al.*, "Formamidinium lead halide perovskite crystals with unprecedented long carrier dynamics and diffusion length," ACS Energy Lett. **1**, 32 (2016).

16. T. Y. Wei, C. T. Huang, B. J. Hansen, *et al.*, "Large enhancement in photon detection sensitivity via Schottky-gated CdS nanowire nanosensors," Appl. Phys. Lett. **96**, 013508 (2010).

17. Y. Ye, L. Dai, X. N. Wen, *et al.*, "High-performance single CdS nanobelt metal-semiconductor field-effect transistor-based photodetectors," ACS Appl. Mater. Interf. **2**, 2724 (2010).

18. J. S. Jie, W. J. Zhang, Y. Jiang, *et al.*, "Photoconductive characteristics of single-crystal CdS nanoribbons," Nano Lett. **6**, 1887 (2006).

19. W. K. Bae, L. A. Padilha, Y. S. Park, *et al.*, "Controlled alloying of the core-shell interface in CdSe/CdS quantum dots for suppression of auger recombination," ACS Nano **7**, 3411 (2013).

20. L. D. Li, Z. Lou, H. R. Chen, *et al.*, "Stretchable $SnO_2$-CdS interlaced-nanowire film ultraviolet photodetectors," Sci. China-Mater. **62**, 1139 (2019).

21. B. H. Liu, M. K. Li, W. Fu, *et al.*, "High-performance self-driven ultraviolet photodetector based on $SnO_2$ p-n homojunction," Opt. Mater. **129**, 112571 (2022).

22. J. Q. Huang, Q. H. Tan, Z. J. Zhang, *et al.*, "Photoconductive properties of Er-CdSe nanobelt detectors," J. Mater. Sci. **54**, 560 (2019).

23. Y. Ye, L. Dai, X. N. Wen, *et al.*, "High-performance single CdS nanobelt metal-semiconductor field-effect transistor-based photodetectors," ACS Appl. Mater. Interfaces **2**, 2724 (2010).

24. V. K. Sharma, R. Mukhopadhyay, A. Mohanty, *et al.*, "Contrasting behaviors of FA and MA cations in $APbBr_3$," J. Phys. Chem. Lett. **11**, 9669 (2020).

25. Y. H. Kim, C. Wolf, Y. T. Kim, *et al.*, "Highly efficient light-emitting diodes of colloidal metal–halide perovskite nanocrystals beyond quantum size," ACS Nano **11**, 6586 (2017).

26. J. Zhang, X. K. Yang, H. Deng, *et al.*, "Low-dimensional halide perovskites and their advanced optoelectronic applications," Nano-Micro Lett. **9**, 26 (2017).

27. W. Zheng, F. Huang, R. S. Zheng, *et al.*, "Low-dimensional structure vacuum-ultraviolet-sensitive ($\lambda < 200$ nm) photodetector with fast-response speed based on high-quality AlN micro/nanowire," Adv. Mater. **27**, 3921 (2015).

28. Z. P. Lian, Q. F. Yan, Q. R. Lv, *et al.*, "High-performance planar-type photodetector on (100) facet of $MAPbI_3$ single crystal," Sci. Rep. **5**, 16563 (2015).

29. B. Nafradi, "Comment on 'Superior photodetectors based on all-inorganic perovskite $CsPbI_3$ nanorods with ultrafast response and high stability,'" ACS Nano **12**, 10570 (2018).

30. D. J. Yu, F. Cao, Y. L. Shen, *et al.*, "Dimensionality and interface engineering of 2D homologous perovskites for boosted charge-carrier transport and photodetection performances," J. Phys. Chem. Lett. **8**, 2565 (2017).

31. F. Y. Zhang, B. Yang, K. B. Zheng, *et al.*, "Formamidinium lead bromide ($FAPbBr_3$) perovskite microcrystals for sensitive and fast photodetectors," Nano-Micro Lett. **10**, 8 (2018).

32. R. Pan, H. Y. Li, J. Wang, *et al.*, "High-responsivity photodetectors based on formamidinium lead halide perovskite quantum dot-graphene hybrid," Part. Part. Syst. Charact. **35**, 1700304 (2018).

33. H. Zhou, Z. Song, C. Wang, *et al.*, "Double coating for the enhancement of the performance in a $MA_{0.7}FA_{0.3}PbBr_3$ photodetector," ACS Photonics **5**, 2100 (2018).

34. D. J. Yu, F. Cao, Y. Gu, *et al.*, "Broadband and sensitive two-dimensional halide perovskite photodetector for full-spectrum underwater optical communication," Nano Res. **14**, 1210 (2021).

35. M. M. Furchi, D. K. Polyushkin, A. Pospischil, *et al.*, "Mechanisms of photoconductivity in atomically thin $MoS_2$," Nano Lett. **14**, 6165 (2014).

36. L. Y. Cao, P. Y. Fan, A. P. Vasudev, *et al.*, "Semiconductor nanowire optical antenna solar absorbers," Nano Lett. **10**, 439 (2010).